Interstitial atom-doped NiFe alloy as pre-catalysts boost direct seawater oxygen evolution

Lumin Song [a], Dan Zhang [c], Hongfu Miao [a], Yue Shi [a], Mengna Wang [a], Liang Zhao [a], Tianrong Zhan [a], Jianping Lai [a,*], Lei Wang [a,b,**]

[a] *Key Laboratory Base of Eco-Chemical Engineering, Ministry of Education, International Science and Technology Cooperation Base of Eco-chemical Engineering and Green Manufacturing, College of Chemistry and Molecular Engineering, Qingdao University of Science and Technology, Qingdao 266042, China*
[b] *Shandong Engineering Research Center for Marine Environment Corrosion and Safety Protection, College of Environment and Safety Engineering, Qingdao University of Science and Technology, Qingdao 266042, China*
[c] *Key Laboratory of Catalytic Conversion and Clean Energy in Universities of Shandong Province, School of Chemistry and Chemical Engineering, Qufu Normal University, Qufu, Shandong, 273165, China*

ARTICLE INFO

ABSTRACT

NiFe-based materials are excellent OER electrocatalysts. However, it is difficult to stabilize anions and cations during reconstruction, which also leads to the problem of high valence metals at low levels and poor stability in direct seawater. Herein, we propose the strategy of using interstitial P atom-doped NiFe alloys ($P_{4.8}$-NiFe ANs-400) as pre-catalysts to stabilize anions and cations, thereby promoting the formation of abundant high-valent metal species and excellent activity and stability in direct seawater. The reconstructed $P_{4.8}$-NiFe ANs-400 catalyst generates a large amount of high-valence transition metal Ni^{4+}, which contributed to its low over-potential (214 mV) and long-term stability (100 h) in a seawater electrolyte at 100 mA cm^{-2}. Experiments and theoretical calculations show that the interstitially doped P atoms share the charge around the Fe and the active Ni sites, optimizing the free energy of the OER intermediate and making the chlorine evolution reaction (CER) difficult to proceed.

1. Introduction

Electrocatalytic water splitting is a key technology to convert renewable economic energy [1,2]. However, the sluggish kinetics of oxygen evolution reaction (OER)[3,4] and the shortage of fresh water resources always restrict the development of electrolyzed water technology [5–7]. Hence, the development of efficient OER electrocatalysts in seawater has more practical application value [8–10]. Whereas, compared to electrolyzed freshwater, electrolytic seawater faces challenges such as competition from chlorine evolution reactions (CER) and osmotic corrosion caused by high concentration of Cl⁻.[11] These challenges can lead to corrosion or even deactivation of the OER catalysts [12,13]. Although noble metal Ir and Ru-based electrocatalysts have high OER activity, their high price and instability seriously hinder large-scale application in the future development of green industries

[14–17].

3d-transition metal materials are the most popularly used OER electrocatalysts among non-precious metals [18–20]. Most importantly, 3d-transition metal-based catalysts are reconstructed to oxides/hydroxyl oxides on the surface under anodic polarization, which automatically optimize the catalytic active site and improve water oxidation [21,22]. In fact, the polarization-activated hydroxyloxides with concentrated high-valence transition metal sites (such as Ni^{IV}, Co^{IV}, Fe^{IV}) are the most active OER electrocatalysts [23]. However, the anions in the catalysts of transition metal-based compounds are readily replaced by oxygen in the electrolyte prior to the formation of the reconstructed active component, which dissolves in the electrolyte, leading to a reduction in the content of the anionic element to less than 0.1% and ultimately preventing the formation of the abundant high valence transition metal. For example, the reconstruction of $Ni_3S_2/Fe-Ni_xP$ heterojunction catalyst is

accompanied by the leaching of anions (S, P) and cations [24]. The reconstruction of Fe-NiSOH precatalyst is accompanied by the complete leaching of S anions (atomic ratio is only 0.08%) [25]. None of the above studies generated a large number of high valence transition metals in seawater enviroment. Also, cations that have lost their anionic support also dissolve readily, especially in highly corrosive seawater environments. Therefore, it is difficult to stabilize anions and cations during reconstruction, which also leads to the problem of high valence metals at low levels and poor stability in direct seawater.

Herein, we propose the strategy of using interstitial atom-doped alloys as pre-catalysts to stabilize anions and cations, thereby promoting the formation of abundant high-valent metal species and excellent stability in direct seawater. Experiments show that the insertion of interstitial P atoms into NiFe alloy nanosheet arrays almost avoids significant leaching of Fe and P atoms in strongly corrosive seawater and increases the content of high-valence metal Ni^{4+}, thereby improving OER activity and stability. Theoretical calculations show that the interstitially doped P atom shares the charge around the Fe site and the active Ni site through its own electron-absorbing ability, prompting the formation of the high-valence metal Ni^{4+} while optimising the free energy of the OER intermediate, making CER difficult. Fe enhances the OER activity of the catalyst mainly by regulating the electronic structure of Ni. During the OER process, the formation of NiOOH requires little exchange of P with O, thus inhibiting the massive dissolution of P element. While Fe is retained in large quantities due to its predominant presence in the core of the reconstructed catalyst.

2. Experimental materials and synthesis

2.1. Materials

Nickel (II) nitrate hexahydrate ($Ni(NO_3)_2 \cdot 6H_2O$, 98%) purchased from Xilong Chemical. Iron (III) nitrate nonahydrate ($Fe(NO_3)_3 \cdot 9H_2O$, 98%, Macklin), urea ($CO(NH_2)_2$), 99%, Aladdin), ammonium fluoride (NH_4F, 98%, Macklin), sodium hypophosphite (NaH_2PO_2, 99%, Aladdin), ammonium carbonate ($(NH_4)_2CO_3$, 99%, Macklin), potassium hydroxide (KOH, 95%, Macklin), and NF of 1.5 mm thickness.

2.2. Preparation of precursor NiFe LDH nanosheets

First, the NF with 3 M HCl and acetone soaking treatment, take out dry for use. Then, 0.84 mmol Ni ($NO_3)_2 \cdot 6$ H_2O, 0.36 mmol Fe ($NO_3)_3 \cdot 9H_2O$, 2.6 mmol NH_4F and 6 mmol CO ($NH_2)_2$ were dissolved in 30 mL deionized water, and the mixed solution was placed in 50 mL polytetrafluoroethylene reactor. The treated NF was placed vertically and reacted at 120 °C for 5 h. The excess sample on the NF was rinsed with deionized water after the reaction. Finally, it was dried in a vacuum drying chamber.

2.3. Preparation of $P_{2.54}$-NiFe ANs-400, $P_{4.8}$-NiFe ANs-400, $P_{12.9}$-NiFe ANs-400

NF (1 cm × 1 cm) for growing NiFe LDH is placed in the downstream of the pipe furnace, and 500 mg sodium hypophosphite is placed in the upstream of the pipe furnace, heated at 400 °C for 2 h under 10% H_2/Ar atmosphere. Get $P_{4.8}$-NiFe ANs-400. The mass of sodium hypophosphite is changed to 300 mg and 700 mg, other conditions remain unchanged, $P_{2.54}$-NiFe ANs-400 and $P_{12.9}$-NiFe ANs-400 are obtained, respectively.

2.4. Preparation of P_x-NiFe ANs-350, P_x-NiFe ANs-450

The heating temperature of the pipe furnace to 350 °C and 450 °C, other conditions are consistent with the main material ($P_{4.8}$-NiFe ANs-400), $P_{4.2}$-NiFe ANs-350 and $P_{5.1}$-NiFe ANs-450 are obtained, respectively.

2.5. Preparation of NiFe ANs-400

NF (1 cm × 1 cm) for growing NiFe LDH is placed in a pipe furnace, heated at 400 °C for 2 h under 10% H_2/Ar atmosphere.

2.6. Preparation of $N_{1.4}$-NiFe ANs-400, $N_{3.5}$-NiFe ANs-400 and $N_{7.8}$-NiFe ANs-400

NF (1 cm × 1 cm) for growing NiFe LDH was placed in the downstream of the pipe furnace, and 400 mg of ammonium carbonate is placed in the upstream of the pipe furnace, heated at 400 °C for 2 h under 10% H_2/Ar atmosphere. Get $N_{3.5}$-NiFe ANs-400. The mass of ammonium carbonate is changed to 300 mg and 700 mg, other conditions remain unchanged, $N_{1.4}$-NiFe ANs-400 and $N_{7.8}$-NiFe ANs-400 are obtained, respectively.

3. Results and discussion

3.1. Synthesis and characterization of P_x-NiFe ANs-Y catalysts

We first grew lamellar NiFe layered double hydroxide (LDH) (Fig. S2) on treated NF (Fig. S1) by hydrothermal method, and then successfully synthesized NiFe alloy nanosheet arrays inserted with interstitial P atoms (P_x-NiFe ANs-Y, X is the mass percentage of phosphorus content, Y is the annealing temperature) by low temperature thermal reduction and atomic diffusion (Scheme 1). By optimizing the amount of phosphorus inserted, main catalyst ($P_{4.8}$-NiFe ANs-400) is obtained. For comparison, the NiFe ANs-400 was synthesized without the addition of a phosphorus source. The atomic ratio of Ni/Fe in NiFe ANs-400 catalyst is 80.5: 19.5 (Table S1). The X-ray diffraction (XRD) pattern of the NiFe ANs-400 shows three diffraction peaks, which are negatively shifted compared to those produced by the (111), (200) and (202) crystal planes of the face-centered cubic (fcc) metallic Ni (PDF# 04–0850). The absence of the characteristic peaks of Fe is due to its low content relative to Ni, which makes the overall crystal structure of the NiFe ANs-400 determined by the metallic Ni of the fcc phase.[26,27] The diffraction peaks of the $P_{4.8}$-NiFe ANs-400 exhibit only a shift toward lower angles and no excess diffraction peaks compared to the NiFe ANs-400, suggesting that the P atoms are inserted into the lattice of the NiFe ANs-400, contributing to a larger lattice spacing (Fig. 1a). The crystal structure parameters of the prepared $P_{4.8}$-NiFe ANs-400 were obtained by Rietveld refinement (Fig. S3), and the results were very consistent with the Fm-3 m structure, the P atoms are in interstitial positions in the NiFe alloy with an occupancy of about 4.8%. Scanning electron microscopy (SEM) images show that the $P_{4.8}$-NiFe ANs-400 catalyst is nanosheet array-like structure (Fig. 1b). Comparing the NiFe LDH (Fig. S2b), the annealed NiFe ANs-400 (Fig. S4a) and $P_{4.8}$-NiFe ANs-400 catalysts have significantly rougher nanosheets. The transmission electron microscopy (TEM) image of $P_{4.8}$-NiFe ANs-400 shows the catalyst as a lamellar structure (Fig. 1c), which is consistent with the SEM image results. High resolution transmission electron microscopy (HRTEM) images show a lattice spacing of 0.218 nm for $P_{4.8}$-NiFe ANs-400 at the (111) crystal plane (Fig. 1d). This is an increase of 0.014 nm compared to the lattice spacing of NiFe ANs-400 on the (111) crystal plane (0.204 nm, Fig. S4b), which is consistent with the XRD pattern being shifted towards a small angle. Fig. 1e clearly shows the presence of heteroatoms by atomic size. In addition, high angle annular dark field scanning transmission electron microscope (HAADF-STEM) and elemental mapping clearly show that Ni, Fe and P elements are present and uniformly distributed in the catalyst (Fig. 1f), which reinforces the successful insertion of P atoms into the catalyst.[28,29] The content ratio of Ni: Fe: P determined by ICP-MS is 77.8: 17.4: 4.8 (Table S2).

In order to analyze the surface chemical state of each element in the catalyst, X-ray Photoelectron Spectroscopy (XPS) were performed on NiFe ANs-400 and $P_{4.8}$-NiFe ANs-400, respectively. The elemental content ratio shown by XPS spectra is similar to the ICP-MS results. As
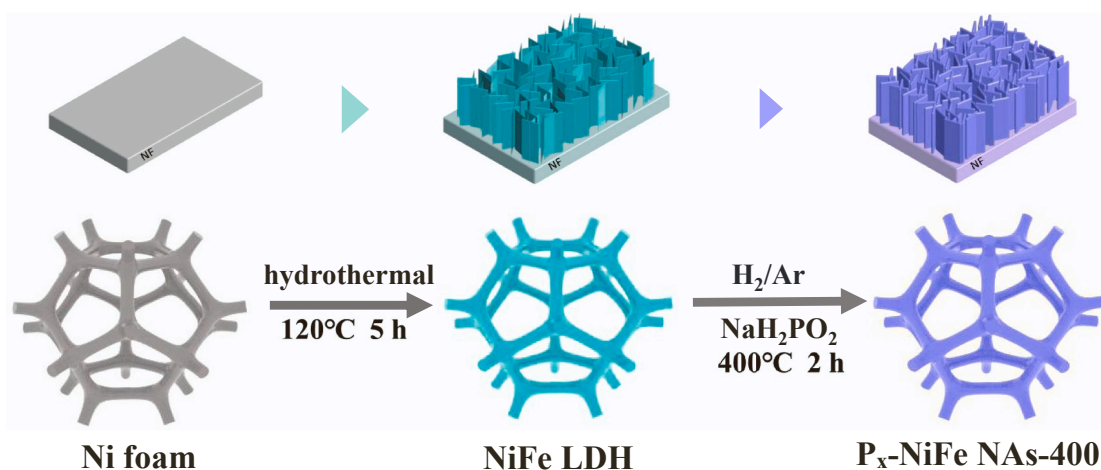
Scheme 1. The synthesis process of P_x-NiFe ANs-400.
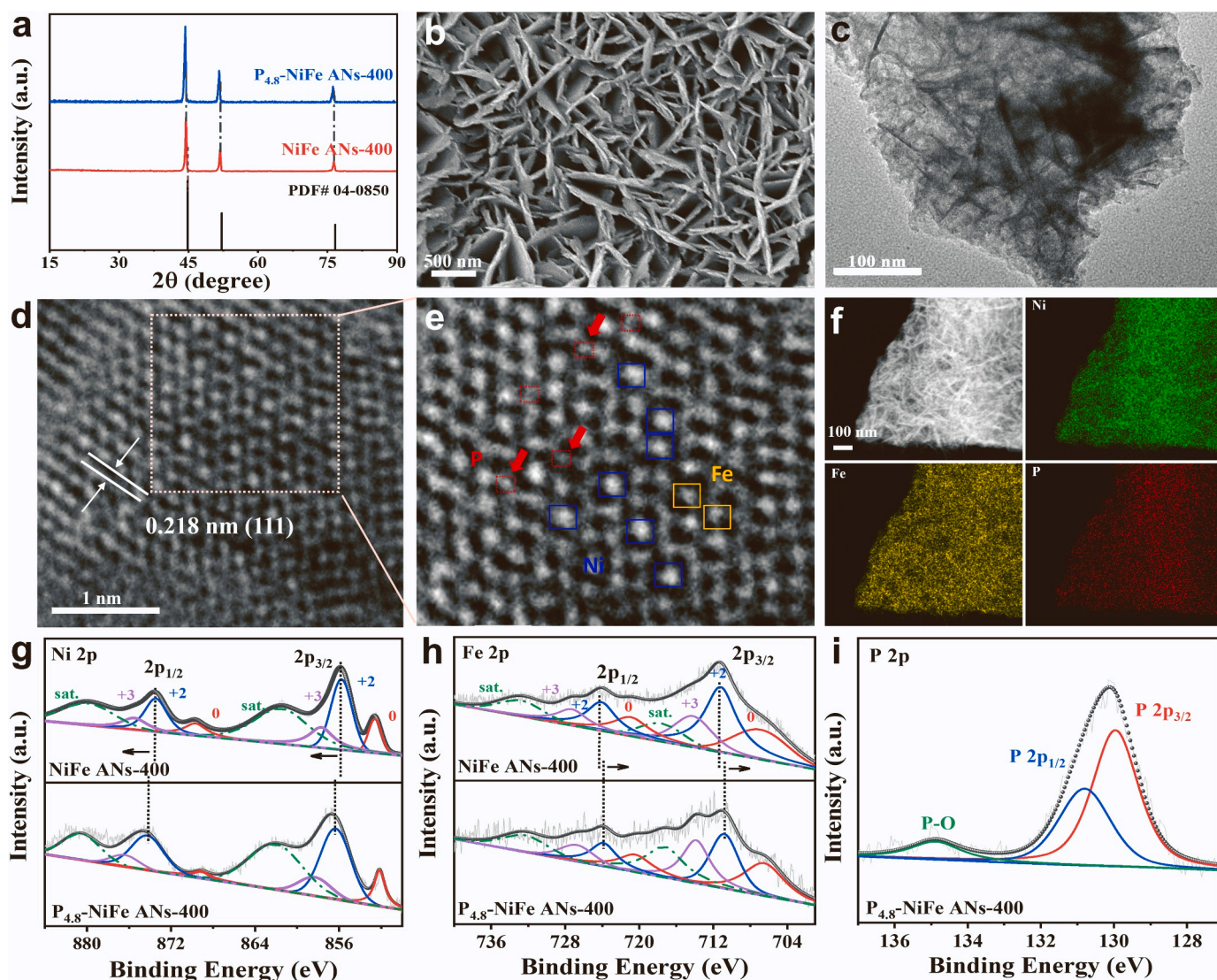
Fig. 1. (a) XRD image of $P_{4.8}$-NiFe ANs-400 catalyst. (b) SEM image of $P_{4.8}$-NiFe ANs-400 catalyst. (c) TEM image of $P_{4.8}$-NiFe ANs-400 catalyst. (d) HRTEM image of $P_{4.8}$-NiFe ANs-400 catalyst. (e) enlarged HRTEM image of $P_{4.8}$-NiFe ANs-400 catalyst. (f) EDX mapping images of $P_{4.8}$-NiFe ANs-400 for Ni, Fe and P, respectively. (g) XPS spectra of Ni 2p and (h) Fe 2p of NiFe ANs-400 and $P_{4.8}$-NiFe ANs-400. (i) XPS spectra of P 2p of $P_{4.8}$-NiFe ANs-400.

shown in Fig. 1g, the Ni 2p spectrum of $P_{4.8}$-NiFe ANs-400 has two peaks at 869.2 eV and 852.1 eV, attributed to Ni^0 $2p_{1/2}$ and Ni^0 $2p_{3/2}$, respectively;[30] 874.2 eV and 856.4 eV belong to Ni^{2+} $2p_{1/2}$ and Ni^{2+} $2p_{3/2}$, respectively,[31] and the peaks at 876.5 eV and 858.5 eV belong to Ni^{3+} $2p_{1/2}$ and Ni^{3+} $2p_{3/2}$, respectively.[32] The presence of the oxidation state may be caused by the long-term exposure of the catalyst to air.[33] The Ni 2p spectrum of $P_{4.8}$-NiFe ANs-400 undergoes a 0.5 eV positive shift compared to that of the NiFe ANs-400. The Fe 2p spectrum of $P_{4.8}$-NiFe ANs-400 shows that the main peaks at 720.6 eV and 706.6 eV belong to Fe^0 $2p_{1/2}$ and Fe^0 $2p_{3/2}$, respectively;[34,35] the peaks located at 723.8 eV and 710.8 eV are corresponding to Fe^{2+} $2p_{1/2}$ and Fe^{2+} $2p_{3/2}$, respectively;[36] 727.0 eV and 713.9 eV belong to Fe^{3+} $2p_{1/2}$ and Fe^{3+} $2p_{3/2}$, respectively,[32,37] and the two peaks present at 717.4 eV and 732.7 eV belong to the satellite peaks of Fe 2p (Fig. 1h). In contrast, the Fe 2p spectrum of $P_{4.8}$-NiFe ANs-400 has a negative shift of 0.2 eV compared to the NiFe ANs-400, indicating a significant charge transfer between Ni and Fe.[33] Secondly, the peak at 134.7 eV in the P 2p spectrum of $P_{4.8}$-NiFe ANs-400 is attributed to P-O; the peaks at 130.8 eV and 129.9 eV belong to P^0 $2p_{1/2}$ and P^0 $2p_{3/2}$, respectively, which is negatively shifted by 0.2 eV compared to the $2p_{3/2}$ peak position (130.1 eV) of red phosphorus.[28] This indicates that the P atoms are mainly used in the catalyst as electron acceptor (Fig. 1i). Therefore, the interstitial doping of P atoms enhance the interaction between Ni and Fe. In short, the presence of a large area of zero-valent states in the XPS spectrum of Ni/Fe indicates that the $P_{4.8}$-NiFe ANs-500 catalyst exists mainly as an alloy. Furthermore, the presence of P elements in the XPS spectra, the negatively shifted diffraction peaks in the XRD pattern, and the increased lattice spacing presented in the HRTEM images indicate that the P atoms are successfully doped into the skeleton of the NiFe ANs-400.[38].

3.2. Electrochemical performance of catalysts in alkaline freshwater

Hydroxyoxides are the real catalytic active sites of NiFe-based catalysts, which have been confirmed by many studies. The doping of interstitial phosphorus atoms effectively improve the catalytic activity of NiFe-based catalysts by optimizing the electronic structure. Therefore, we investigated the OER performance of reconstructed $P_{4.8}$-NiFe ANs-400 and its contrast sample in a 1.0 M KOH electrolytewe to verify the role of interstitial-phosphorus atoms in regulating the electronic structure. Electrochemical measurement uniformly uses a three-electrode system, and cyclic voltammetry (CV) activation is performed before testing. The reconstructed $P_{4.8}$-NiFe ANs-400 catalyst was then subjected to a linear scanning voltammetry (LSV) curve test. From Fig. 2a, it can be observed that reconstructed $P_{4.8}$-NiFe ANs-400 have the most excellent OER performance. At current densities of 100 mA cm^{-2} and 500 mA cm^{-2}, the reconstructed $P_{4.8}$-NiFe ANs-400 (244 mV and 291 mV) have the smallest overpotential compared to reconstructed NiFe ANs-400 (285 mV and 342 mV), reconstructed NiFe LDH (302 mV and 356 mV) (Fig. 2b) and even better than that of commercial RuO_2 (341 mV and 486 mV). Meanwhile, the Tafel slope of reconstructed $P_{4.8}$-NiFe ANs-400 (34.3 mV dec^{-1}) is smaller than that of reconstructed NiFe ANs-400 (45.4 mV dec^{-1}), reconstructed NiFe LDH (47.3 mV dec^{-1}) and commercial RuO_2 (89.1 mV dec^{-1}) (Fig. 2c), indicating that the reconstructed $P_{4.8}$-NiFe ANs-400 catalyst has excellent OER kinetics. In addition, the reconstructed $P_{4.8}$-NiFe ANs-400 and their comparison samples were subjected to electrochemical impedance spectroscopy (EIS) (Fig. 2d). Among them, the reconstructed $P_{4.8}$-NiFe ANs-400 has the smallest charge transfer resistance, which proves that the insertion of P atoms can accelerate the charge transfer of reconstructed NiFe ANs-400. It is well known that the amount of P insertion and the reduction temperature have a great influence on all aspects of the catalysts. Therefore, we first adjust the annealing temperature of the catalyst according to the bearing temperature of nickel foam. When the annealing temperature is 350 ℃ (Fig. S5a), the poor activity of the OER may be due to the reduced specific surface area of the catalyst due to the smooth edges of the nanosheets. When the annealing temperature reaches 450 ℃ (Fig. S5b), many cracks appear on the surface of nickel foam, leading to poor activity and stability of the catalyst. Therefore, we found that the morphology and toughness of the catalyst at 400 ℃ is more
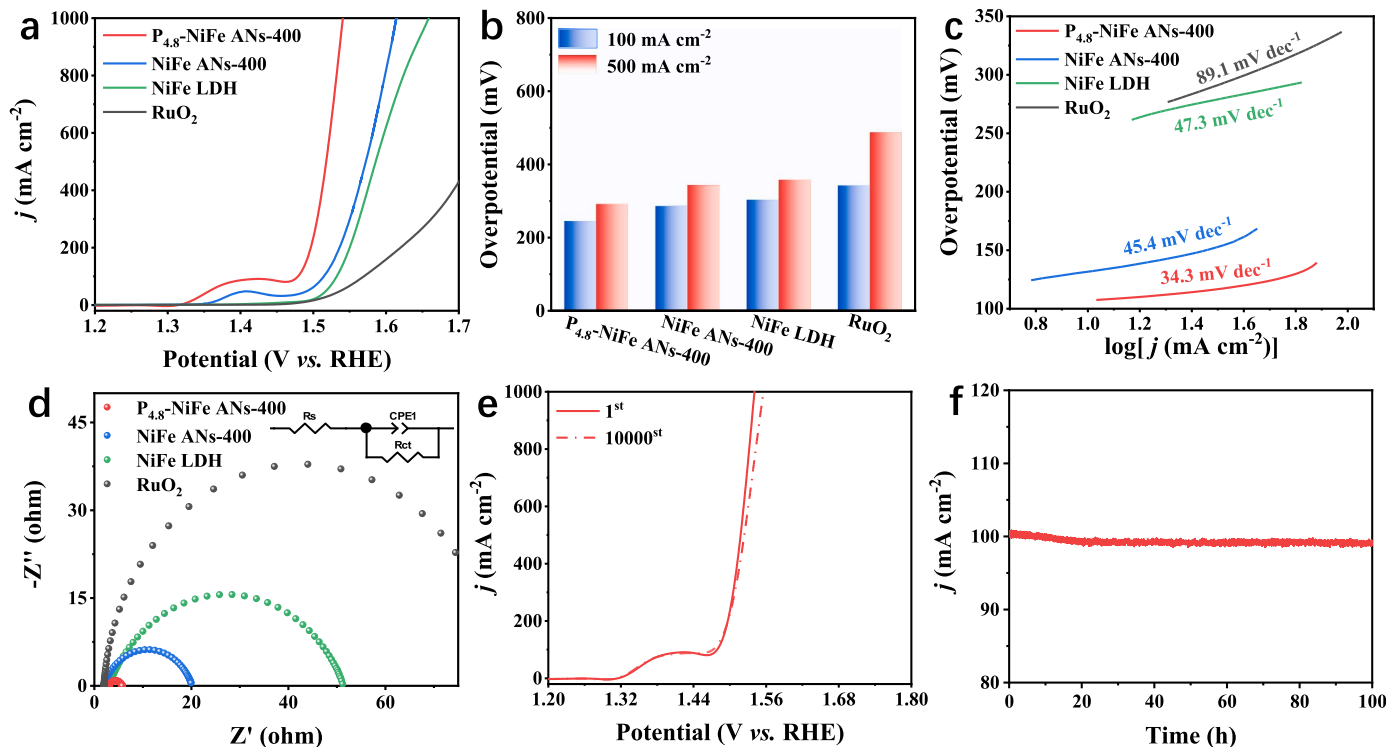

Fig. 2. (a) OER polarization curves. (b) Overpotential comparison at 100 mA cm^{-2} and 500 mA cm^{-2}. (c) Tafel plots obtained from the polarization curves in (a). (d) Nyquist plots. (e) Polarization curves for $P_{4.8}$-NiFe ANs-400 catalysts before and after 10,000 cycles. (f) Timing current curve of $P_{4.8}$-NiFe ANs-400 at 100 mA cm^{-2}.

suitable. Secondly, we prepared $P_{2.54}$-NiFe ANs-400, $P_{12.9}$-NiFe ANs-400 by varying the addition of sodium hypophosphite while fixing other reaction conditions, respectively. Table S3 is shown as the P content in the catalyst measured by ICP-MS test. The XRD patterns are shown in Fig. S6, and it can be seen that only $P_{12.9}$-NiFe ANs-400 catalyst formed phosphide. This may be caused by the addition of too much sodium hypophosphite.[10,39] The electrochemical performance of the catalysts were tested in 1.0 M KOH electrolyte with varying phosphorus content and temperature, and Fig. S7a and c show the polarization curves of the catalysts. The comparative overpotential of the catalysts at different current densities (Fig. S7b and d) show that the reconstructed $P_{4.8}$-NiFe ANs-400 catalyst has the lowest value. This proves that the reconstructed NiFe ANs-400 catalyst only at P insertion of 4.8 wt% and annealing temperature of 400 ℃ has the most excellent OER performance. Analyzed from the perspective of phosphorus content, when P content is less than 4.8 wt% ($P_{2.54}$-NiFe ANs-400, Fig. S5c), the catalyst has poor OER performance due to inappropriate electronic regulation and poor corrosion resistance.[40] When the phosphorus content reaches 12.9 wt% ($P_{12.9}$-NiFe ANs-400, Fig. S5d), the excessive P leads to the complete destruction of the catalyst lamellar structure, resulting in the formation of phosphate. The $P_{12.9}$-NiFe ANs-400 catalyst at this point will have a large amount of phosphate leaching during the reaction, thus covering the catalytic active site.[40] Besides, we performed stress and strain analyses on catalysts with different P doping amounts and found that the degree of strain along the xx direction of the $P_{4.8}$-NiFe ANs-400 catalyst was nearly 80% (Fig. S8a). When the doping amount was increased, the $P_{12.9}$-NiFe ANs-400 catalyst formed a phosphide and no strain was generated; when the doping amount was reduced, the $P_{2.45}$-NiFe ANs-400 catalyst had a localized strain degree of nearly 50% along the xx direction (Fig. S8b). This suggests that the interstitial doping amount can regulate the strain degree of the catalysts and thus enhance the catalytic performance. In conclusion, the appropriate P insertion amount and temperature can not only regulate the electronic structure of the catalyst stably and effectively, but also effectively improve the OER activity and stability of the catalyst.

To further explore the OER activity of the catalysts, the CV curves of the catalysts at different scan rates were tested (Fig. S9a-**c**). The double layer capacitance (C_{dl}) of the catalyst are obtained from the CV curves data. As shown in Fig. S9d, the C_{dl} of reconstructed $P_{4.8}$-NiFe ANs-400 is 6.85 mF cm^{-2}, which is larger than that of reconstructed NiFe ANs-400 (5.44 mF cm^{-2}) and the reconstructed NiFe LDH (2.71 mF cm^{-2}). For this reason, the electrochemically active surface area (ECSA) of the reconstructed $P_{4.8}$-NiFe ANs-400 catalyst (42.81 cm^2) is also larger than that of the reconstructed NiFe ANs-400 (34.00 cm^2) and reconstructed NiFe LDH (16.93 cm^2) (Fig. S10a). Meanwhile, the reconstructed $P_{4.8}$-NiFe ANs-400 catalyst also has the largest number of active sites (n) (Fig. S10b). This may be caused by the increased surface roughness of the catalyst after annealing. To elucidate the intrinsic activity of the catalyst, the turnover frequency (TOF) value (4.41 s^{-1}) of reconstructed $P_{4.8}$-NiFe ANs-400 catalyst at 300 mV was further derived, which is superior to that of reconstructed NiFe ANs-400 (1.24 s^{-1}) and reconstructed NiFe LDH (1.34 s^{-1}) (Fig. S11). It is thus known that the insertion of P atoms can significantly improve the intrinsic activity of the reconstructed $P_{4.8}$-NiFe ANs-400 catalyst. In addition, well stabilization is essential for the catalyst. As shown in Fig. 2e, the overpotential of reconstructed $P_{4.8}$-NiFe ANs-400 decayed by only 7 mV at a current density of 500 mA cm^{-2} after 10,000 CV cycles. At the same time, the reconstructed $P_{4.8}$-NiFe ANs-400 catalyst was tested for up to 100 h in 1.0 M KOH, and it is finally found that the reconstructed $P_{4.8}$-NiFe ANs-400 catalyst has no significant attenuation at a constant current density of 100 mA cm^{-2} (Fig. 2f). These results show that the reconstructed $P_{4.8}$-NiFe ANs-400 catalyst has long-term durability in alkaline fresh water.

3.3. Electrochemical performance of catalysts in alkaline seawater

Since seawater accounts for 97.5% of the earth's water resources,

about 35 times that of fresh water. Thus, the use of seawater instead of freshwater for electrocatalytic oxygen production has a more practical application value. Considering that the reconstructed $P_{4.8}$-NiFe ANs-400 catalyst has excellent OER activity in alkaline fresh water, we further configured a simulated seawater (1.0 M KOH + 0.6 M NaCl) electrolyte to test the performance of the catalyst (Fig. 3a). As shown in Fig. 3b, the overpotentials of the reconstructed $P_{4.8}$-NiFe ANs-400 catalyst at 500 mA cm^{-2} and 1000 mA cm^{-2} current densities are 293 mV and 325 mV, respectively, indicating that the catalyst is able to maintain excellent OER activity in the simulated seawater. Further, we used the seawater from Trestle Bridge in Shibei District, Qingdao City, Shandong Province as the electrolyte for testing the LSV curves of the catalysts (Fig. 3c). The OER performance of reconstructed $P_{4.8}$-NiFe ANs-400 remains the most outstanding compared to reconstructed NiFe ANs-400 and reconstructed NiFe LDH. Fig. 3d shows that the overpotentials of reconstructed $P_{4.8}$-NiFe ANs-400 at 100 mA cm^{-2}, 300 mA cm^{-2} and 500 mA cm^{-2} are 214 mV, 273 mV and 305 mV, respectively, which are lower than those of reconstructed NiFe ANs-400 (294 mV, 347 mV, 373 mV), reconstructed NiFe LDH (352 mV, 383 mV, 401 mV) and recently reported NiFe-based catalysts in the literature (Table S4). However, the potential of reconstructed $P_{4.8}$-NiFe ANs-400 at 100 mA cm^{-2} is disturbed by the oxidation peak and is less exact. In a word, the overpotential of the reconstructed $P_{4.8}$-NiFe ANs-400 catalyst in seawater is only 17 mV (500 mA cm^{-2}) higher than that in fresh water, which proves that the catalyst also has excellent OER activity in seawater. Besides, the overpotential (355 mV, 1000 mA cm^{-2}) of reconstructed $P_{4.8}$-NiFe ANs-400 catalyst at seawater does not exceed 480 mV (the theoretical potential for chlorine evolution), which is theoretically insufficient to trigger CER. In order to analyze whether the catalyst occurs CER, we tested the oxygen evolution content of reconstructed $P_{4.8}$-NiFe ANs-400 using gas chromatography (GC) and calculated the Faraday efficiency (FE) of the catalyst at 1 h. The FE of oxygen evolution for reconstructed $P_{4.8}$-NiFe ANs-400 in seawater electrolyte is finally found to be close to 100% (Fig. 3f), which implies that the catalyst can effectively suppress CER.[41] Moreover, we tested the generation of hypochlorite in seawater electrolyte by a simple method. For comparison. We analyzed seawater before the reaction and deionized water following the same method. The results showed that no light yellow precipitation appeared in deionized water, seawater and after seawater, which indicated the absence ClO⁻ in all three solutions (Fig. S12). Among them, Cl⁻ exists in seawater and after seawater, which is reasonable. Finally, the intrinsic activity of the catalyst in seawater is evaluated by TOF. Fig. S13 shows that the TOF of the reconstructed $P_{4.8}$-NiFe ANs-400 catalyst is 2.65 s^{-1} at an overpotential of 300 mV, which is much higher than that of the reconstructed NiFe ANs-400 (0.82 s^{-1}), reconstructed NiFe LDH (0.63 s^{-1}) and other catalysts reported in the literature (Table S5). Thus, the insertion of P atoms in the reconstructed NiFe ANs-400 makes the reconstructed $P_{4.8}$-NiFe ANs-400 catalyst more prone to OER in seawater.

3.4. Stability characterization

We performed a series of stability tests on the reconstructed $P_{4.8}$-NiFe ANs-400 catalyst. First, the reconstructed $P_{4.8}$-NiFe ANs-400 was tested in an electrolyte of seawater for up to 100 h at time-ampere (Fig. 3e), and the catalyst showed no significant rise and fall at 100 mA cm^{-2}. In addition, we tested the structural stability of after reconstructed $P_{4.8}$-NiFe ANs-400. Due to the poor crystallinity of NiOOH, no characteristic peaks of NiOOH is detected in the after XRD pattern (Fig. S14).[36] After SEM image demonstrates that the lamellar structure of the reconstructed $P_{4.8}$-NiFe ANs-400 catalyst is not destroyed and a thin film is formed on its surface (Fig. S15). In order to explore the stability of P in the catalyst, XPS spectra and phosphorus content determination are carried out on the reconstructed $P_{4.8}$-NiFe ANs-400 catalyst after reaction. First, after the P 2p spectrum (Fig. S16) shows the presence of P and the area of P-O peaks increases significantly. The ICP-MS shows that the P content
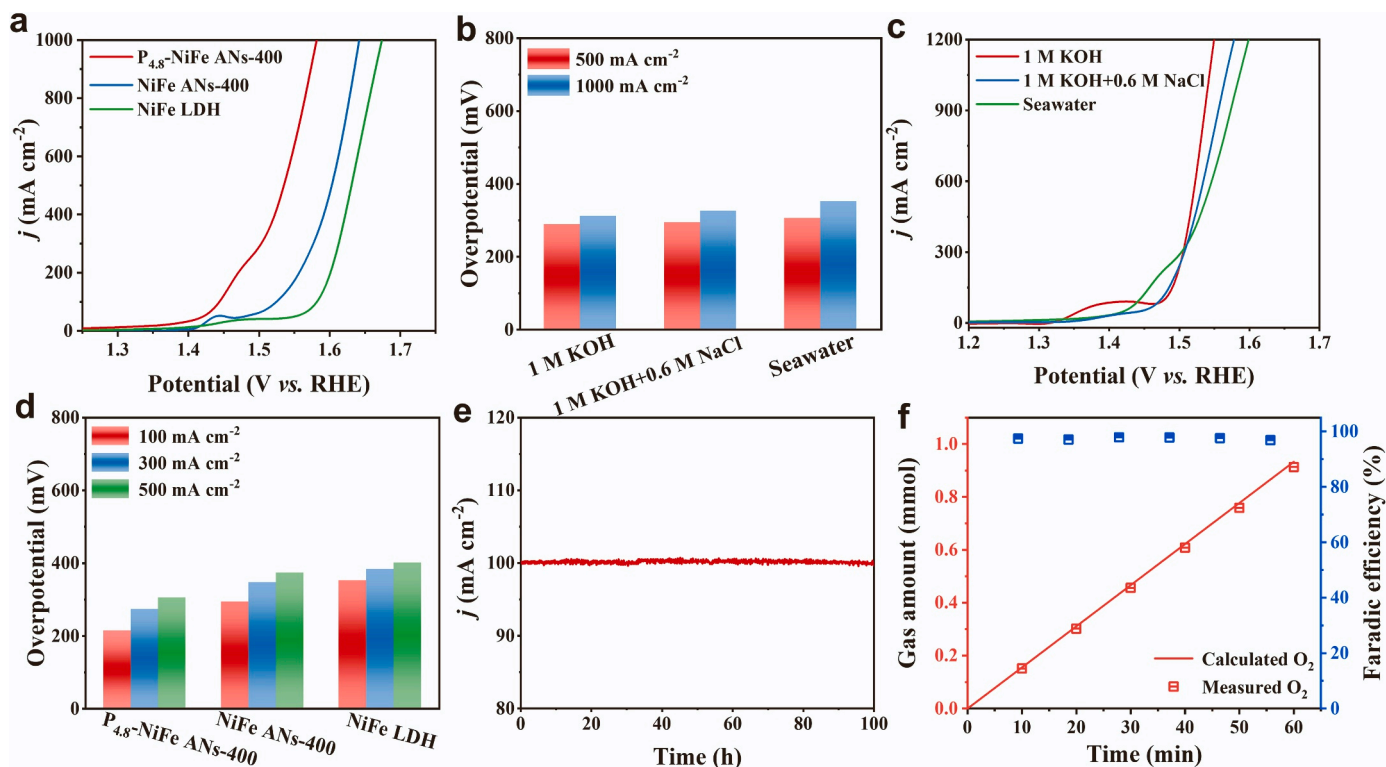
Fig. 3. (a) OER polarization curves and (b) overpotential comparison of $P_{4.8}$-NiFe ANs-400 catalysts in different solution. (c) OER polarization curves and (d) overpotential comparison of $P_{4.8}$-NiFe ANs-400, NiFe ANs-400 and NiFe LDH catalysts in seawater solution. (e) Timing of current curve of $P_{4.8}$-NiFe ANs-400 catalysts in seawater solution. (f) FE and O_2 Production of $P_{4.8}$-NiFe ANs-400 catalysts in seawater solution.
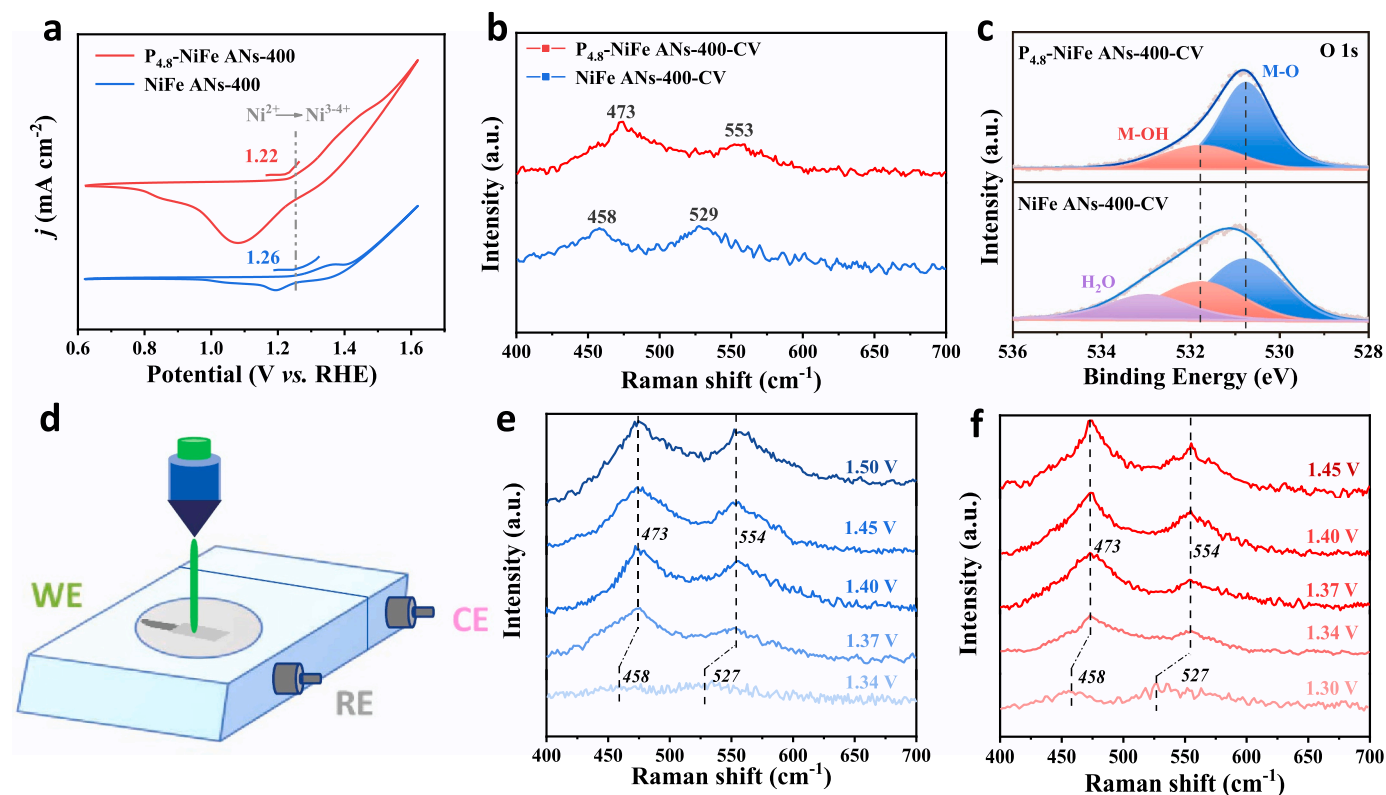

Fig. 4. (a) Redox pairs after activation of $P_{4.8}$-NiFe ANs-400 and NiFe ANs-400, with enlarged illustrations representing the initial oxidation potential from Ni^{2+} to Ni^{3-4+}. (b) Raman spectra and (c) O 1 s XPS spectra of the $P_{4.8}$-NiFe ANs-400 and NiFe ANs-400 catalysts after CV activation. (d) Schematic diagram of an in situ Raman device. (e) In situ Raman spectra of NiFe ANs-400 catalysts in seawater solution. (f) In situ Raman spectra of $P_{4.8}$-NiFe ANs-400 catalysts in seawater solution.

before and after the reaction is basically maintained around 4.1 wt% (Fig. S17), which is consistent with the after P 2p spectrum test results. The above results reasonably verify the long-term stability of the reconstructed $P_{4.8}$-NiFe ANs-400 catalyst. Above all, interstitially doped phosphorus can be present in large quantities in the catalyst, stably and effectively regulating the electronic structure of the active site. This is also an important reason why the reconstructed $P_{4.8}$-NiFe ANs-400 catalyst stands out.

3.5. Formation of high-valence metals

It is worth noting that the addition of phosphorus atoms makes the OER activity of the catalyst have a great advantage. This change is worth further study. Firstly, the redox behavior of the two catalysts are analyzed. As shown in Fig. 4**a**, the initial potential of the oxidation of $P_{4.8}$-NiFe ANs-400 from Ni^{2+} to Ni^{3-4+} is 1.22 V, 40 mV lower than that of NiFe ANs-400. Further, raman spectroscopy are performed on the catalysts after CV cycle (denoted as $P_{4.8}$-NiFe ANs-400-CV and NiFe ANs-400-CV). Fig. 4b shows that NiOOH has been formed on the surface of $P_{4.8}$-NiFe ANs-400-CV, while NiFe ANs-400-CV only has a characteristic peak of $Ni(OH)_2$, suggesting that $P_{4.8}$-NiFe ANs-400 catalyst has time-saving and efficient reconstruction characteristics. In addition, the O 1 s spectra after activation show that the M-O/M-OH peaks area ratio of $P_{4.8}$-NiFe ANs-400-CV is 2.72, which is much higher than that of NiFe ANs-400-CV (1.46) (Fig. 4c). This suggests that $P_{4.8}$-NiFe ANs-400-CV has more hydroxides converted to hydroxyl oxides. The Ni 2p spectra after the reaction are shown in Fig. S18a. Compared with reconstructed NiFe ANs-400, the Ni 2p XPS spectrum of reconstructed $P_{4.8}$-NiFe ANs-400 shows a positive shift of about 0.2 eV, indicating that reconstructed $P_{4.8}$-NiFe ANs-400 has a higher valence state, thus forming more Ni^{3-4+}. This is also consistent with the results shown in Fig. S18b. The disappearance of Ni^0 and the increase in the Ni^{3+} area compared to before $P_{4.8}$-NiFe ANs-400 indicate the formation of a dense NiOOH film on the surface of the after $P_{4.8}$-NiFe ANs-400 catalyst (Fig. S19a). This is consistent with the after SEM (Fig. S15). Interestingly, Fe^0 was still present in the after Fe 2p spectra (Fig. S19b), implying that Fe had not been completely oxidized. Secondly, during the oxidation process, only the characteristic peaks of NiOOH were present in the in situ Raman spectra (Fig. 4f), and no FeOOH was detected, which rationalized the presence of Fe^0. Then, to explore the real catalytically active phase of the catalyst, we used in situ Raman spectroscopy (Fig. 4d) to dissect the dynamic reconstruction of the catalyst surface. Fig. 4f shows the dynamic plot of the $P_{4.8}$-NiFe ANs-400 catalyst with the gradual increase of the applied voltage. When the applied voltage is 1.30 V, two Raman bands appear at 458 cm^{-1} and 527 cm^{-1}, which are attributed to the Ni-OH and Ni-O vibrational bands of Ni(OH), respectively.[42] When the applied voltage was increased to 1.34 V, the two vibrational bands of Ni(OH) were red-shifted to 473 cm^{-1} and 554 cm^{-1}, belong to the δ(Ni-O) vibrational band and ν(Ni-O) stretching vibrational band of NiOOH.[43] After greater than 1.37 V, the position of the Raman band does not change and the Ni-O vibration peak of NiOOH at 554 cm^{-1} gradually increases. When the applied voltage is 1.40 V, the intensity ratio of δ(Ni-O) and ν(Ni-O) peaks tends to be stable. It should be noted that there is no Raman band about Fe in the range of 300 cm^{-1} to 700 cm^{-1}, and it is reasonable to assume that this is due to low Fe content,[44–46] equating to Fe being present as a dopant. Due to the loose structure of γ-NiOOH, its peak intensity (ratio of δ(Ni-O) to ν(Ni-O) is denoted as $I_{\delta/\nu}$) is higher than that of β-NiOOH.[45] Meanwhile, the average valence of Ni in γ-NiOOH is 3.7, indicating the presence of highly oxidized Ni^{4+} species.[25,47] Importantly, the $P_{4.8}$-NiFe ANs-400 catalyst has a peak-intensity ratio of 1.7–2.1 at different potentials, indicating the formation of a γ-NiOOH of Ni^{4+} (Table S6). In addition, comparing the in situ Raman spectra of $P_{4.8}$-NiFe ANs-400 and NiFe ANs-400 (Fig. 4e), it can be observed that the γ-NiOOH of the $P_{4.8}$-NiFe ANs-400 catalyst appears at a lower potential (1.34 V) than that of the active phase of the NiFe ANs-400 (1.37 V), indicating the insertion of P reduces the

formation barrier of NiOOH and promotes the reconstruction of active species.[42] Finally, we conducted HRTEM image on the reacted $P_{4.8}$-NiFe ANs-400 and found that an oxide layer appeared at the edge of the catalyst (Fig. S20, inside the black dashed line). Furthermore, Fig. S21 shows that the lattice spacing of the $P_{4.8}$-NiFe ANs-400 surface is consistent with the (105) crystallographic plane of γ-NiOOH, which is consistent with the results tested with in situ Raman spectroscopy. Therefore, it can be speculated that the insertion of P induced the formation of more highly oxidized Ni^{4+} in the $P_{4.8}$-NiFe ANs-400 catalyst.

3.6. Characterization and electrocatalytic performance testing of N_x-NiFe ANs-400 catalyst

To broaden the practical applicability of the catalyst preparation method and stabilization of the regulated electronic structure. Under other conditions unchanged, we prepared NiFe ANs-400 interstitial nanosheet arrays with N inserted (N_x-NiFe ANs-400) using ammonium carbonate instead of phosphorus source. Due to the limitation of the temperature at which NF can withstand, we obtained 400 °C as the most suitable temperature from the above P-doping study. In order to explore the appropriate amount of N doping, we synthesized catalysts with different doping amounts. Next, electrochemical tests were performed on the N_x-NiFe ANs-400 catalysts. The $N_{3.5}$-NiFe ANs-400 catalyst has the best catalytic performance as shown in Fig. S22. From a microscopic point of view, the GPA geometrical phase diagram of the $N_{3.5}$-NiFe ANs-400 and $N_{7.8}$-NiFe ANs-400 catalysts along the xx direction show strong localized tensile strain (Fig. S23a, b). However, the $N_{1.4}$-NiFe ANs-400 catalyst shows only 10% degree of strain along the xx direction (Fig. S23c). It is evident that strain plays a key role in the factors affecting catalyst activity. The atomic ratio of $N_{3.5}$-NiFe ANs-400 catalyst was determined by ICP-MS as 77.7: 18.8: 3.5 (Table S7). The XRD pattern of $N_{3.5}$-NiFe ANs-400 (Fig. S24) shows that the diffraction peak of the catalyst is shifted in the direction of larger lattice spacing, and there are no other characteristic peaks compared with NiFe ANs-400. SEM image showes that the morphology of $N_{3.5}$-NiFe ANs-400 remains as an array of nanosheets (Fig. S25), the insertion of N did not change the morphology of the precursors. Meanwhile, the XPS spectra contain N element. So, it can be assumed that the N atoms are interstitially inserted into the NiFe ANs-400. XPS spectra characterize the chemical state of each element in the catalyst. As with the $P_{4.8}$-NiFe ANs-400 catalyst, Fe 2p spectrum of $N_{3.5}$-NiFe ANs-400 is negatively shifted by 0.42 eV compared to that of NiFe ANs-400, where Fe acts as an electron acceptor in the catalyst and there is a significant charge transfer between Ni and Fe. In the N 2p spectrum, the characteristic peak at 398.3 eV is attributed to pyridine nitrogen,[48] that is, N-Ni/Fe; the characteristic peak at 400.1 eV is due to N_2 chemisorbed by the catalyst;[33] and the characteristic peak at 406.4 eV is oxidized nitrogen, which is caused by slight oxidation of the catalyst surface when placed in air (Fig. S26c).[49] Furthermore, we electrochemically tested the reconstructed $N_{3.5}$-NiFe ANs-400 catalyst under alkaline conditions. Fig. S27a shows that the overpotential of reconstructed $N_{3.5}$-NiFe ANs-400 (283 mV) at 100 mA cm^{-2} current density is 58 mV lower than that of RuO_2 (Fig. S27b). The tafel slope of reconstructed $N_{3.5}$-NiFe ANs-400 (45.2 mV dec^{-1}) is 43.9 mV dec^{-1} lower than that of RuO_2 (Fig. S27c). To evaluate the charge transfer capability of reconstructed $N_{3.5}$-NiFe ANs-400, we tested the EIS of reconstructed $N_{3.5}$-NiFe ANs-400. Fig. S27d shows that the charge transfer resistance of reconstructed $N_{3.5}$-NiFe ANs-400 is 4.6 Ω, which is 18 times lower than that of RuO_2 (83.5 Ω). In addition, we evaluated the electrochemical active area of the catalyst by calculating a series of data (Fig. S28-31). Meanwhile, the TOF of reconstructed $N_{3.5}$-NiFe ANs-400 under 1.0 M KOH condition is 1.43 at 300 mV (Fig. S32). It can be seen that the insertion of N can also enhance the intrinsic activity of reconstructed $N_{3.5}$-NiFe ANs-400. The stability of reconstructed $N_{3.5}$-NiFe ANs-400 is a factor that must be considered as an electrocatalyst. Finally, we have performed XRD pattern, SEM image, and XPS spectra on after reconstructed

N$_{3.5}$-NiFe ANs-400. As shown in Fig. S33, no overall change occurred in XRD pattern. SEM image shows the appearance of holes on the surface of the nanosheets, but the overall structure did not collapse (Fig. S34). After XPS spectra show that the zero valence states of Ni and Fe remained (Fig. S35a and b), indicating that the dynamics of the surface reconstruction of the N$_{3.5}$-NiFe ANs-400 differed from that of the P$_{4.8}$-NiFe ANs-400, and the exact changes remain to be explored. The N element remains in the catalyst after the reaction (Fig. S35c), indicating that the atoms inserted into the lattice are not easily dissolved in the electrolyte. Furthermore, we tested the content of N and P in the N$_{3.5}$-NiFe ANs-400 and P$_{4.8}$-NiFe ANs-400 catalysts before and after stabilization by ICP-MS, the results showed that there were a few dissolved of both N and P atoms, but the effect on the catalyst as a whole was negligible (Fig. S36). It is verified that the method of stabilization of the interstitial atoms to regulate the electronic structure is also applicable to other reconstructed catalysts.

3.7. Theoretical calculations

According to the above introduction, both NiFe ANs-400 and P$_{4.8}$-NiFe ANs-400 nanosheet catalysts on the surface are reconstructed to form NiOOH during the activation process. The NiOOH on the surface and the P$_{4.8}$-NiFe ANs-400 catalyst in the core are one and the same. Therefore, the theoretical models constructed in the analysis of the role of phosphorus atoms in the catalytic activity by DFT calculations are the optimized structures of NiFe ANs-400/NiOOH (Fig. S37a) and P$_{4.8}$-NiFe ANs-400/P-NiOOH (Fig. S37b). CER uses the Volmer-Heyrovsky mechanism[50] in this paper, which mainly includes the adsorption process of Cl$^-$ (i.e. Volmer step) and the binding process of intermediate Cl* with Cl$^-$ (i.e. Heyrovsky step). The oxygen-containing intermediates included in the four-electron transfer process of OER under alkaline conditions are *OH, *O, *OOH. Calculations show that the rate-determining step (RDS) of NiFe ANs-400/NiOOH catalyst is *O→*OOH (ΔG=1.93 eV) (Fig. 5a). However, the insertion of P atoms changes the RDS and decreases the formation energy of *OOH. Meanwhile, the adsorption free energy of P$_{4.8}$-NiFe ANs-400/P-NiOOH RDS (ΔG_{*O-*OH} =1.78 eV) is smaller than that of NiFe ANs-400/NiOOH catalyst, indicating that the insertion of P atoms significantly optimize the adsorption free energy of

the OER intermediates and enhanced the P$_{4.8}$-NiFe ANs-400/P-NiOOH catalyst's intrinsic activity (Fig. 5c). For CER, the weak adsorption of Cl$^-$ by NiFe ANs-400/NiOOH completely hinders the late Heyrovsky step. The insertion of P atoms, although lowering the adsorption free energy (ΔG=2.21 eV) for the CER rate-determining step, still can not change the weak adsorption of Cl$^-$ by P$_{4.8}$-NiFe ANs-400/P-NiOOH itself (Fig. 5b, d). Meanwhile, the OER theoretical overpotential of P$_{4.8}$-NiFe ANs-400/P-NiOOH is smaller than that of CER, which indicates that it is theoretically more favorable for OER to occur. In short, the interstitial doping of P atoms successfully promotes the OER kinetics of the catalyst and fundamentally inhibits the CER directly. Fig. S38 presents the charge density difference of P$_{4.8}$-NiFe ANs-400/P-NiOOH, which shows that the P and Fe atoms are electron-rich regions. The insertion of P atoms enhanced the stability of Fe ions, redistributed the charge of the catalyst, induced the oxidation of Ni^{2+} to Ni^{3-4+}, and effectively regulated the electronic structure of P$_{4.8}$-NiFe ANs-400/P-NiOOH. In short, the insertion of P atoms can optimize the adsorption energy of OER intermediates by stably and effectively adjusting the electronic structure of the catalyst, increase the number of high-valence species and improve the performance of OER.

3.8. AEM electrolysis

In view of the excellent OER activity and stability of P$_{4.8}$-NiFe ANs-400 catalyst, we further explored the application potential of P$_{4.8}$-NiFe ANs-400 catalyst with a loading of 0.04 mg cm^{-2} in water electrolysis. Since the hydrogen evolution reaction (HER) performance of P$_{4.8}$-NiFe ANs-400 catalyst is higher than that of Pt/C, we operated P$_{4.8}$-NiFe ANs-400 loaded on nickel foam as anode and cathode, respectively, in an practical AEM electrolyzer at 60 °C (Fig. 6a and b). Fig. 6c shows that the water-splitting activity of the P$_{4.8}$-NiFe ANs-400||P$_{4.8}$-NiFe ANs-400 electrolyzer can easily reach 1.0 A cm^{-2} at a voltage of 1.876 V, which is significantly better than that of the commercial Pt/C||RuO$_2$. Next, we evaluated the stability of the P$_{4.8}$-NiFe ANs-400||P$_{4.8}$-NiFe ANs-400 electrolyzer. Fig. 6d shows that the P$_{4.8}$-NiFe ANs-400||P$_{4.8}$-NiFe ANs-400 couple showed almost no change in voltage for 500 h of continuous operation at a current density of 1.0 A cm^{-2}, while Pt/C||RuO$_2$ as a comparison, under the same test conditions, showed a voltage down.
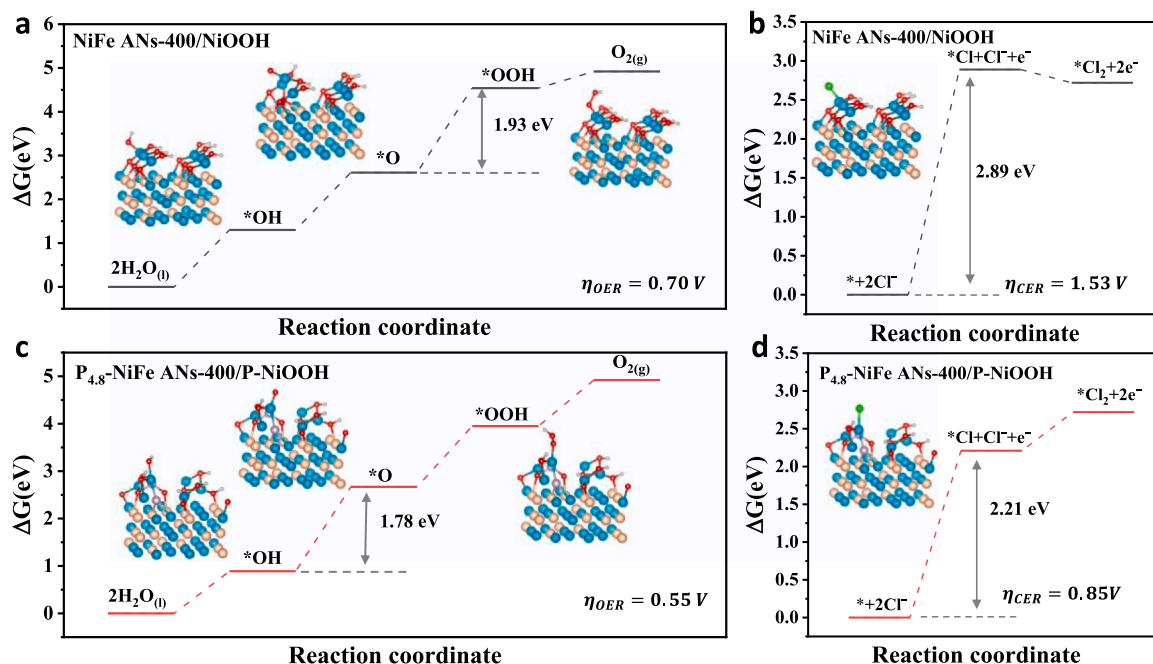

Fig. 5. (a, c) Calculate the Gibbs free energy required during the four-electron reaction of the OER intermediate and (b, d) the two-electron reaction of the CER intermediateat U= 0 V$_{RHE}$. Ni, Fe, P, O, and H are represented by blue, orange, purple, red and gray, respectively.
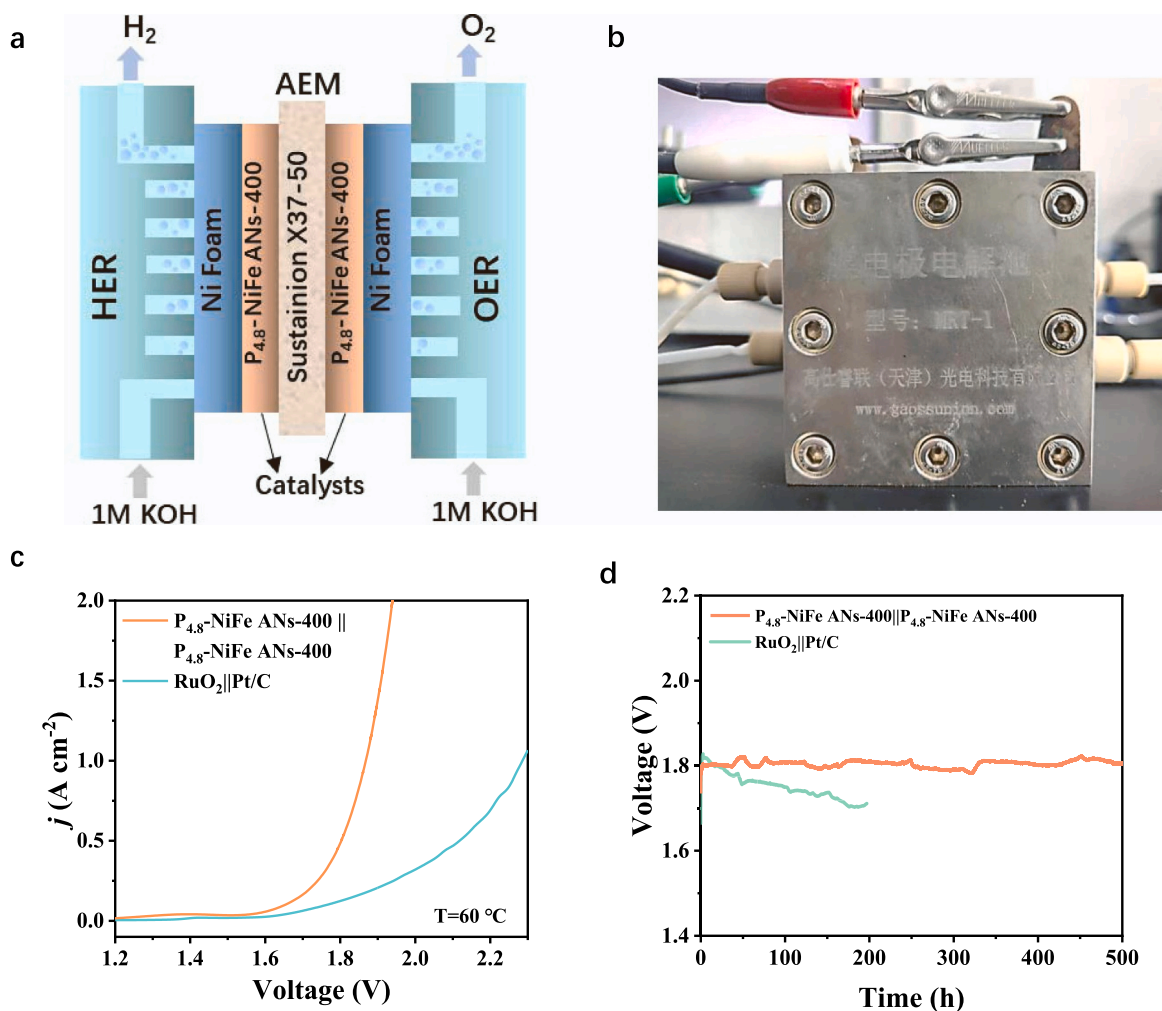
Fig. 6. (a) Schematic diagram and (b) picture of AEM electrolyzer. (c) Polarization curve of $P_{4.8}$-NiFe ANs-400||$P_{4.8}$-NiFe ANs-400 couple during electrolysis, at the temperature of 60 ℃. (d) Chronopotentiometry curves of $P_{4.8}$-NiFe ANs-400||$P_{4.8}$-NiFe ANs-400 and RuO_2||Pt/C during AEM electrolysis.

These results clearly demonstrate the great potential of non-precious $P_{4.8}$-NiFe ANs-400 catalysts for future practical applications.

4. Conclusions

In summary, we demonstrate that the interstitially doped phosphorus atoms and Fe can stably exist in the $P_{4.8}$-NiFe ANs-400 catalyst, and through its own electron-absorbing ability promote the stable formation of more high-valent metal sites Ni^{4+} (15.18%), showing excellent OER activity and stability in seawater. In direct seawater, the overpotential of only 214 mV are required at a current density of 100 mA cm^{-2}. The high TOF is 2.65 s^{-1} at 300 mV, which was a great improvement compared with other NiFe based catalysts. Besides, the FE of the OER in seawater is close to 100%. At a constant current density of 100 mA cm^{-2}, reconstructed $P_{4.8}$-NiFe ANs-400 show excellent OER durability, with no significant increase in potential after 100 h of testing. In particular, the AEM electrolytic cell constructed with $P_{4.8}$-NiFe ANs-400 as anode and cathode catalyst shows great potential for practical applications, as it can work stably for over 500 h at 1.8 V. DFT calculations indicate that the insertion of large amounts of P optimises the free energy of the OER intermediates, making it difficult for CER to proceed. This strategy of interstitial atom-doped alloys as pre-catalysts can be used to generate other efficient reconstructed catalysts.

CRediT authorship contribution statement

Lei Wang and **Jianping Lai** supervised the research. **Jianping Lai** conceived the research. **Jianping Lai** and **Lumin Song** designed the experiments. **Lumin Song** performed most of the experiments and data analysis. **Dan Zhang**, **Hongfui Miao** and **Yue Shi** prepared the electrodes and helped with electrochemical measurements. **Mengna Wang**, **Liang Zhao** and **Tianrong Zhan** helped answer some questions. All authors discussed the results and commented on the manuscript.

Declaration of Competing Interest

The authors declare no competing financial interests.

Data Availability

Data will be made available on request.

Acknowledgement

Appendix A. Supporting information

Supplementary data associated with this article can be found in the online version at doi:10.1016/j.apcatb.2023.123376.

References

[1] S. Lee, K. Banjac, M. Lingenfelder, X. Hu, Oxygen isotope labeling experiments reveal different reaction sites for the oxygen evolution reaction on nickel and nickel iron oxides, Angew. Chem. Int. Ed. 58 (2019) 10295–10299, https://doi.org/10.1002/anie.201903200.

[2] B. Zhang, X. Zheng, O. Voznyy, R. Comin, Homogeneously dispersed, multimetal oxygen-evolving catalysts, Science 352 (2016) 333–337, https://doi.org/10.1126/science.aaf1525.

[3] C.C. McCrory, S. Jung, I.M. Ferrer, S.M. Chatman, J.C. Peters, T.F. Jaramillo, Benchmarking hydrogen evolving reaction and oxygen evolving reaction electrocatalysts for solar water splitting devices, J. Am. Chem. Soc. 137 (2015) 4347–4357, https://doi.org/10.1021/ja510442p.

[4] A.A.H. Tajuddin, M. Wakisaka, T. Ohto, Y. Yu, H. Fukushima, H. Tanimoto, X. Li, Y. Misu, S. Jeong, J.I. Fujita, H. Tada, T. Fujita, M. Takeguchi, K. Takano, K. Matsuoka, Y. Sato, Y. Ito, Corrosion-resistant and high-entropic non-noble-metal electrodes for oxygen evolution in acidic media, Adv. Mater. 35 (2023), e2207466, https://doi.org/10.1002/adma.202207466.

[5] J. Hao, W. Luo, S. Wang, K. Zhao, J. Hou, L. Li, B. Ge, W. Yang, W. Shi, Discharge-induced enhancement of the oxygen evolution reaction, Angew. Chem. Int. Ed. 60 (2021) 20042–20048, https://doi.org/10.1002/anie.202108770.

[6] J.T. Mefford, A.R. Akbashev, M. Kang, C.L. Bentley, W.E. Gent, H.D. Deng, D. H. Alsem, Y.S. Yu, N.J. Salmon, D.A. Shapiro, P.R. Unwin, W.C. Chueh, Correlative operando microscopy of oxygen evolution electrocatalysts, Nature 593 (2021) 67–73, https://doi.org/10.1038/s41586-021-03454-x.

[7] N. Nie, D. Zhang, Z. Wang, W. Yu, S. Ge, J. Xiong, Y. Gu, B. Yang, J. Lai, L. Wang, Stable PtNb-Nb2O5 heterostructure clusters @CC for high-current-density neutral seawater hydrogen evolution, Appl. Catal. B Environ. 318 (2022), https://doi.org/10.1016/j.apcatb.2022.121808.

[8] D. Zhang, H. Miao, X. Wu, Z. Wang, H. Zhao, Y. Shi, X. Chen, Z. Xiao, J. Lai, L. Wang, Scalable synthesis of ultra-small Ru2P@Ru/CNT for efficient seawater splitting, Chin. J. Catal. 43 (2022) 1148–1155, https://doi.org/10.1016/s1872-2067(21)64012-3.

[9] S. Dresp, F. Dionigi, S. Loos, J. Ferreira de Araujo, C. Spöri, M. Gliech, H. Dau, P. Strasser, Direct electrolytic splitting of seawater: activity, selectivity, degradation, and recovery studied from the molecular catalyst structure to the electrolyzer cell level, Adv. Energy Mater. 8 (2018), e1800338, https://doi.org/10.1002/aenm.201800338.

[10] C. Lyu, J. Cheng, K. Wu, J. Wu, N. Wang, Z. Guo, P. Hu, W.-M. Lau, J. Zheng, Interfacial electronic structure modulation of CoP nanowires with FeP nanosheets for enhanced hydrogen evolution under alkaline water/seawater electrolytes, Appl. Catal. B Environ. 317 (2022), 121799, https://doi.org/10.1016/j.apcatb.2022.121799.

[11] J. Guo, Y. Zheng, Z. Hu, C. Zheng, J. Mao, K. Du, M. Jaroniec, S.-Z. Qiao, T. Ling, Direct seawater electrolysis by adjusting the local reaction environment of a catalyst, Nat. Energy 8 (2023) 264–272, https://doi.org/10.1038/s41560-023-01195-x.

[12] T. Lim, J.H. Kim, J. Kim, D.S. Baek, T.J. Shin, H.Y. Jeong, K.-S. Lee, K.S. Exner, S. H. Joo, General efficacy of atomically dispersed Pt catalysts for the chlorine evolution reaction: potential-dependent switching of the kinetics and mechanism, ACS Catal. 11 (2021) 12232–12246, https://doi.org/10.1021/acscatal.1c03893.

[13] L. Zhuang, J. Li, K. Wang, Z. Li, M. Zhu, Z. Xu, Structural buffer engineering on metal oxide for long-term stable seawater splitting, Adv. Funct. Mater. 32 (2022) 2201127, https://doi.org/10.1002/adfm.202201127.

[14] S. Chen, H. Huang, P. Jiang, K. Yang, J. Diao, S. Gong, S. Liu, M. Huang, H. Wang, Q. Chen, Mn-doped RuO2 nanocrystals as highly active electrocatalysts for enhanced oxygen evolution in acidic media, ACS Catal. 10 (2019) 1152–1160, https://doi.org/10.1021/acscatal.9b04922.

[15] Z. Chen, H. Yang, S. Mebs, H. Dau, M. Driess, Z. Wang, Z. Kang, P.W. Menezes, Reviving oxygen evolution electrocatalysis of bulk La-Ni intermetallics via gaseous hydrogen engineering, Adv. Mater. (2022), e2208337, https://doi.org/10.1002/adma.202208337.

[16] K. Deng, Q. Mao, W. Wang, P. Wang, Z. Wang, Y. Xu, X. Li, H. Wang, L. Wang, Defect-rich low-crystalline Rh metallene for efficient chlorine-free H2 production by hydrazine-assisted seawater splitting, Appl. Catal. B Environ. 310 (2022), https://doi.org/10.1016/j.apcatb.2022.121338.

[17] S. Liu, S. Ren, R.-T. Gao, X. Liu, L. Wang, Atomically embedded Ag on transition metal hydroxides triggers the lattice oxygen towards sustained seawater electrolysis, Nano Energy 98 (2022), 107212, https://doi.org/10.1016/j.nanoen.2022.107212.

[18] H. Yang, L. Gong, H. Wang, C. Dong, J. Wang, K. Qi, H. Liu, X. Guo, B.Y. Xia, Preparation of nickel-iron hydroxides by microorganism corrosion for efficient oxygen evolution, Nat. Commun. 11 (2020) 5075, https://doi.org/10.1038/s41467-020-18891-x.

[19] Z. He, J. Zhang, Z. Gong, H. Lei, D. Zhou, N. Zhang, W. Mai, S. Zhao, Y. Chen, Activating lattice oxygen in NiFe-based (oxy)hydroxide for water electrolysis, Nat. Commun. 13 (2022) 2191, https://doi.org/10.1038/s41467-022-29875-4.

[20] H. You, D. Wu, D. Si, M. Cao, F. Sun, H. Zhang, H. Wang, T.F. Liu, R. Cao, Monolayer NiIr-layered double hydroxide as a long-lived efficient oxygen evolution catalyst for seawater splitting, J. Am. Chem. Soc. 144 (2022) 9254–9263, https://doi.org/10.1021/jacs.2c00242.

[21] D. Li, W. Wan, Z. Wang, H. Wu, S. Wu, T. Jiang, G. Cai, C. Jiang, F. Ren, Self-derivation and surface reconstruction of Fe-doped Ni3S2 electrode realizing high-efficient and stable overall water and urea electrolysis, Adv. Energy Mater. 12 (2022), e2201913, https://doi.org/10.1002/aenm.202201913.

[22] N. Zhang, X. Feng, D. Rao, X. Deng, L. Cai, B. Qiu, R. Long, Y. Xiong, Y. Lu, Y. Chai, Lattice oxygen activation enabled by high-valence metal sites for enhanced water oxidation, Nat. Commun. 11 (2020) 4066, https://doi.org/10.1038/s41467-020-17934-7.

[23] Q. Wu, J. Liang, M. Xiao, C. Long, L. Li, Z. Zeng, A. Mavric, X. Zheng, J. Zhu, H. W. Liang, H. Liu, M. Valant, W. Wang, Z. Lv, J. Li, C. Cui, Non-covalent ligand-oxide interaction promotes oxygen evolution, Nat. Commun. 14 (2023) 997, https://doi.org/10.1038/s41467-023-36718-3.

[24] X. Luo, P. Ji, P. Wang, X. Tan, L. Chen, S. Mu, Spherical Ni3S2/Fe-NiPx magic cube with ultrahigh water/seawater oxidation efficiency, Adv. Sci. 9 (2022), e2104846, https://doi.org/10.1002/advs.202104846.

[25] C. Huang, Q. Zhou, D. Duan, L. Yu, W. Zhang, Z. Wang, J. Liu, B. Peng, P. An, J. Zhang, L. Li, J. Yu, Y. Yu, The rapid self-reconstruction of Fe-modified Ni hydroxysulfide for efficient and stable large-current-density water/seawater oxidation, Energ. Environ. Sci. 15 (2022) 4647–4658, https://doi.org/10.1039/d2ee01478e.

[26] H. Xu, B. Liu, J. Liu, Y. Yao, Z.G. Gu, X. Yan, Revealing the surface structure-performance relationship of interface-engineered NiFe alloys for oxygen evolution reaction, J. Colloid Interf. Sci. 622 (2022) 986–994, https://doi.org/10.1016/j.jcis.2022.04.160.

[27] C. Wang, H. Yang, Y. Zhang, Q. Wang, NiFe alloy nanoparticles with hcp crystal structure stimulate superior oxygen evolution reaction electrocatalytic activity, Angew. Chem. Int. Ed. 58 (2019) 6099–6103, https://doi.org/10.1002/anie.201902446.

[28] R. Shi, H.F. Ye, F. Liang, Z. Wang, K. Li, Y. Weng, Z. Lin, W.F. Fu, C.M. Che, Y. Chen, Interstitial P-doped CdS with long-lived photogenerated electrons for photocatalytic water splitting without sacrificial agents, Adv. Mater. 30 (2018), e1705941, https://doi.org/10.1002/adma.201705941.

[29] Z. Li, W. Niu, Z. Yang, N. Zaman, W. Samarakoon, M. Wang, A. Kara, M. Lucero, M. V. Vyas, H. Cao, H. Zhou, G.E. Sterbinsky, Z. Feng, Y. Du, Y. Yang, Stabilizing atomic Pt with trapped interstitial F in alloyed PtCo nanosheets for high-performance zinc-air batteries, Energ. Environ. Sci. 13 (2020) 884–895, https://doi.org/10.1039/c9ee02657f.

[30] D. Lim, E. Oh, C. Lim, S.E. Shim, S.-H. Baeck, Bimetallic NiFe alloys as highly efficient electrocatalysts for the oxygen evolution reaction, Catal. Today 352 (2020) 27–33, https://doi.org/10.1016/j.cattod.2019.09.046.

[31] Y. Zhao, W. Wan, Y. Chen, R. Erni, C.A. Triana, J. Li, C.K. Mavrokefalos, Y. Zhou, G.R. Patzke, Understanding and optimizing ultra-thin coordination polymer derivatives with high oxygen evolution performance, Adv. Energy Mater. 10 (2020), e2002228, https://doi.org/10.1002/aenm.202002228.

[32] Y. Yang, L. Dang, M.J. Shearer, H. Sheng, W. Li, J. Chen, P. Xiao, Y. Zhang, R. J. Hamers, S. Jin, Highly active trimetallic NiFeCr layered double hydroxide electrocatalysts for oxygen evolution reaction, Adv. Energy Mater. 8 (2018), e1703189, https://doi.org/10.1002/aenm.201703189.

[33] W. Yu, H. Huang, Y. Qin, D. Zhang, Y. Zhang, K. Liu, Y. Zhang, J. Lai, L. Wang, The synergistic effect of pyrrolic-N and pyridinic-N with Pt under strong metal-support interaction to achieve high-performance alkaline hydrogen evolution, Adv. Energy Mater. 12 (2022), e2200110, https://doi.org/10.1002/aenm.202200110.

[34] Z.W. Gao, J.Y. Liu, X.M. Chen, X.L. Zheng, J. Mao, H. Liu, T. Ma, L. Li, W.C. Wang, X.W. Du, Engineering NiO/NiFe LDH intersection to bypass scaling relationship for oxygen evolution reaction via dynamic tridimensional adsorption of intermediates, Adv. Mater. 31 (2019), e1804769, https://doi.org/10.1002/adma.201804769.

[35] Q. Xie, D. Ren, L. Bai, R. Ge, W. Zhou, L. Bai, W. Xie, J. Wang, M. Grätzel, J. Luo, Investigation of nickel iron layered double hydroxide for water oxidation in different pH electrolytes, Chin. J. Catal. 44 (2023) 127–138, https://doi.org/10.1016/s1872-2067(22)64190-1.

[36] H. Lei, L. Ma, Q. Wan, S. Tan, B. Yang, Z. Wang, W. Mai, H.J. Fan, Promoting surface reconstruction of NiFe layered double hydroxide for enhanced oxygen evolution, Adv. Energy Mater. 12 (2022), e2202522, https://doi.org/10.1002/aenm.202202522.

[37] J. Zhu, G. Zhao, W. Sun, Q. Nie, S. Wang, Q. Xue, Y. Liu, Y. Lu, Superior FeNi3-FeOx/Ni-foam catalyst for gas-phase hydrogenation of dimethyl oxalate to ethanol, Appl. Catal. B Environ. 270 (2020), 118873, https://doi.org/10.1016/j.apcatb.2020.118873.

[38] J. Zhang, X. Shang, H. Ren, J. Chi, H. Fu, B. Dong, C. Liu, Y. Chai, Modulation of inverse spinel Fe3O4 by phosphorus doping as an industrially promising electrocatalyst for hydrogen evolution, Adv. Mater. 31 (2019), e1905107, https://doi.org/10.1002/adma.201905107.

[39] X. Jin, H. Jang, N. Jarulertwathana, M.G. Kim, S.J. Hwang, Atomically thin holey two-dimensional Ru2P nanosheets for enhanced hydrogen evolution electrocatalysis, ACS Nano 16 (2022) 16452–16461, https://doi.org/10.1021/acsnano.2c05691.

[40] A.R.J. Kucernak, V.N. Naranammalpuram Sundaram, Nickel phosphide: the effect of phosphorus content on hydrogen evolution activity and corrosion resistance in acidic medium, J. Mater. Chem. A 2 (2014) 17435–17445, https://doi.org/10.1039/c4ta03468f.

[41] L. Zhang, Z. Wang, J. Qiu, Energy-saving hydrogen production by seawater electrolysis coupling sulfion degradation, Adv. Mater. 34 (2022), e2109321, https://doi.org/10.1002/adma.202109321.

[42] J. Li, Y. Liu, H. Chen, Z. Zhang, X. Zou, Design of a multilayered oxygen-evolution electrode with high catalytic activity and corrosion resistance for saline water splitting, Adv. Funct. Mater. 31 (2021), e2101820, https://doi.org/10.1002/adfm.202101820.

[43] B. Wu, S. Gong, Y. Lin, T. Li, A. Chen, M. Zhao, Q. Zhang, L. Chen, A unique NiOOH@FeOOH heteroarchitecture for enhanced oxygen evolution in saline water, Adv. Mater. 34 (2022), e2108619, https://doi.org/10.1002/adma.202108619.

[44] L.L. Bai, S. Hu, X, Spectroscopic and electrokinetic evidence for a bifunctional mechanism of the oxygen evolution reaction, Angew. Chem. Int. Ed. 60 (2021) 3095–3103, https://doi.org/10.1002/anie.202011388.

[45] D. Friebel, M.W. Louie, M. Bajdich, K.E. Sanwald, Y. Cai, A.M. Wise, M.J. Cheng, D. Sokaras, T.C. Weng, R. Alonso-Mori, R.C. Davis, J.R. Bargar, J.K. Norskov, A. Nilsson, A.T. Bell, Identification of highly active Fe sites in (Ni,Fe)OOH for electrocatalytic water splitting, J. Am. Chem. Soc. 137 (2015) 1305–1313, https://doi.org/10.1021/ja511559d.

[46] L. Bai, S. Lee, X. Hu, Spectroscopic and electrokinetic evidence for a bifunctional mechanism of the oxygen evolution reaction, Angew. Chem. Int. Ed. 60 (2021) 3095–3103, https://doi.org/10.1002/anie.202011388.

[47] Z. Yan, H. Sun, X. Chen, H. Liu, Y. Zhao, H. Li, W. Xie, F. Cheng, J. Chen, Anion insertion enhanced electrodeposition of robust metal hydroxide/oxide electrodes for oxygen evolution, Nat. Commun. 9 (2018) 2373, https://doi.org/10.1038/s41467-018-04788-3.

[48] C. Deng, K.H. Wu, J. Scott, S. Zhu, R. Amal, D.W. Wang, Core/Shell NiFe nanoalloy with a discrete N-doped graphitic carbon cover for enhanced water oxidation, ChemElectroChem 5 (2018) 732–736, https://doi.org/10.1002/celc.201701285.

[49] S. Wei, C. Wan, L. Zhang, X. Liu, W. Tian, J. Su, W. Cheng, Y. Wu, N-doped and oxygen vacancy-rich $NiCo_2O_4$ nanograss for supercapacitor electrode, Chem. Eng. J. 429 (2022), 132242, https://doi.org/10.1016/j.cej.2021.132242.

[50] H.A. Hansen, I.C. Man, F. Studt, F. Abild-Pedersen, T. Bligaard, J. Rossmeisl, Electrochemical chlorine evolution at rutile oxide (110) surfaces, Phys. Chem. Chem. Phys. 12 (2010) 283–290, https://doi.org/10.1039/b917459a.